

Article

Numerical Equilibrium Configurations and Quadrupole Moments of Post-Merger Differentially Rotating Relativistic Stars

Kevin Franceschetti ^{1,*}, Luca Del Zanna ^{2,3,4}, Jacopo Soldateschi ^{2,3,4} and Niccolò Bucciantini ^{2,3,4}

¹ Dipartimento di Scienze Matematiche Fisiche e Informatiche, Università di Parma, Parco Area delle Scienze 7/A, I-43124 Parma, Italy

² Dipartimento di Fisica e Astronomia, Università degli Studi di Firenze, Via G. Sansone 1, I-50019 Sesto Fiorentino, Italy; luca.delzanna@unifi.it (L.D.Z.); jacopo.soldateschi@unifi.it (J.S.); niccolo.bucciantini@inaf.it (N.B.)

³ INAF, Osservatorio Astrofisico di Arcetri, Largo E. Fermi 5, I-50125 Firenze, Italy

⁴ INFN, Sezione di Firenze, Via G. Sansone 1, I-50019 Sesto Fiorentino, Italy

* Correspondence: kevin.franceschetti@unipr.it

Abstract: Numerical simulations of binary neutron star mergers invariably show that, when a long-lived remnant forms, its rotation profile is never a simple decaying function of the radius but rather exhibits a maximum rotation rate shifted away from the center. This is in contrast to the usual differential rotation profile employed for the numerical modeling of axisymmetric equilibria of relativistic stars. Two families of rotation rate functions that mimic post-merger profiles were proposed by Uryū et al. (2017). In this work we implement Uryū's profiles into the XNS code by Bucciantini and Del Zanna (2011) and we present novel equilibrium sequences of differentially rotating neutron stars. These are constructed by using three different equations of state, in order to study the dependence of mass, radius, angular momentum, and other important physical quantities, especially the quadrupole deformation and metric quadrupole moment, from the rotation properties.

Keywords: neutron stars; differential rotation; numerical methods; magnetohydrodynamic (MHD); relativistic processes



Citation: Franceschetti, K.; Del Zanna, L.; Soldateschi, J.; Bucciantini, N. Numerical Equilibrium Configurations and Quadrupole Moments of Post-Merger Differentially Rotating Relativistic Stars. *Universe* **2022**, *8*, 172. <https://doi.org/10.3390/universe8030172>

Academic Editor: Sergei B. Popov

Received: 8 February 2022

Accepted: 7 March 2022

Published: 9 March 2022

Publisher's Note: MDPI stays neutral with regard to jurisdictional claims in published maps and institutional affiliations.



Copyright: © 2022 by the authors. Licensee MDPI, Basel, Switzerland. This article is an open access article distributed under the terms and conditions of the Creative Commons Attribution (CC BY) license (<https://creativecommons.org/licenses/by/4.0/>).

1. Introduction

On August 2017, the Advanced Virgo detector and the two Advanced LIGO detectors coherently observed a transient gravitational-wave (GW) signal (GW170817) produced by the coalescence of a binary neutron star (BNS) system [1]. This observation, with its electromagnetic counterpart-designated GRB 170817A [2], has set a real milestone in the history of multi-messenger astronomy. The GW spectrum provides a fertile ground for exploring many fundamental questions in physics and astronomy [3].

Numerical relativity simulations have become an irreplaceable tool to study the properties of the merger remnant and the GWs emitted during the coalescence process (e.g., [4–14]). When a long-lived remnant (lifetime of at least 10 ms) forms from a BNS merger, these numerical simulations show that the resulting hypermassive neutron star (HMNS) is supported against collapse toward a black hole by strong differential rotation gradients. The remnant typically presents a rotation profile which is shallow at the center, followed by a rapid increase toward a maximum, located at a few kilometers away from the center, beyond which the rotation rate drops following an almost Keplerian trend. Analytical families of post-merger rotational profiles with the desired properties that mimic the outcome of simulations have been proposed by Uryū et al. (2017) [15] (see also [16] for a different rotation profile and [17] for non-barotropic equilibria).

In order to investigate the physics of BNS remnants and HMNSs, for instance the production of GWs or their further evolution, it is useful to extend the numerical tools to

build equilibria of relativistic stars, usually assuming rigid rotation or simple monotonic profiles (e.g., [18–20]), by also allowing for these remnant-like differential rotation profiles. Recently the mentioned functions proposed by Uryū have been successfully included in existing or novel numerical tools for hydrodynamic equilibria [17,21–25].

In the present work we investigate in detail the properties of BNS merger remnants, here modelled as axisymmetric, stationary, differentially rotating neutron stars, using different families of barotropic (zero temperature) equations of state (EoSs), and assuming the rotation profiles by Uryū. We then show how various physical quantities, such as mass, radius, and angular momentum, and in particular of the quadrupole deformation and metric quadrupole moment, depend on the rotation parameters and on the chosen EoS. All models have been computed using the XNS code [26,27] (<https://www.arcetri.inaf.it/science/ahead/XNS/>, accessed on 5 December 2021), which is derived from the X-ECHO code by Bucciantini and Del Zanna (2011) [26] and solves the general relativistic magnetohydrodynamics (GRMHD) equations together with the Einstein equations, under the *eXtended Conformal Flatness Condition* (XCFC) approximation [28] for the metric. Axisymmetric configurations of relativistic stars obtained with XNS have been extensively studied also in the magnetized case, for non-polytropic tabulated equations of state, and more recently for scalar-tensor extended theories of gravity [19,27,29–32]. The XNS code allows to compute magnetized equilibrium models with poloidal, toroidal and mixed magnetic fields and the implementation of post-merger-like rotational profiles is therefore useful in view of future studies of GRMHD dynamics using the ECHO code [33] or similar.

The paper is organized as follow. In Section 2 we discuss the theoretical framework. In Section 3 we present the main results of our set of models. In Section 4 we summarize and conclude. In Appendix A our implementation of the Uryū rotation profiles in the XNS code is described in details.

Throughout the text we set $c = G = M_{\odot} = 1$, where M_{\odot} is the solar mass, and we assume a signature $(-, +, +, +)$ for the spacetime metric.

2. Theoretical Framework

Under the assumption of stationarity and axisymmetry, the relativistic Euler equation for a rotating non-magnetized fluid in spherical coordinates (t, r, θ, ϕ) can be written as

$$\frac{\nabla p}{\varepsilon + p} - \nabla \ln u^t + j \nabla \Omega = 0 \tag{1}$$

where $u^\mu = (u^t, 0, 0, u^\phi)$ is the fluid four-velocity, ε the total energy density of the fluid, p the (isotropic) pressure, $\Omega = u^\phi / u^t$ the angular velocity, or rotation rate, and $j = u^t u_\phi$ the (gravitationally redshifted) specific angular momentum. For barotropes, i.e., $\varepsilon = \varepsilon(p)$, one can always introduce a (*pseudo*) specific enthalpy function h such that

$$\nabla \ln h = \frac{\nabla p}{\varepsilon + p} \tag{2}$$

so that the integrability condition of Equation (1) turns out to be $j = j(\Omega)$, i.e., j must be a function of the angular velocity alone. One can then integrate Equation (1) using Equation (2) and obtain the generalized Bernoulli integral

$$\ln \frac{h}{u^t} + \int j d\Omega = \mathcal{B} \tag{3}$$

where \mathcal{B} is a constant, usually computed at the center of the star $r = 0$ where j vanishes. Among the many possible rotational laws for $j(\Omega)$, often also indicated with $F(\Omega)$, one of the most commonly adopted (e.g., [26,34–38]) is

$$j(\Omega) = A^2(\Omega_c - \Omega) \tag{4}$$

where A is a constant and Ω_c is the central rotation rate of the star. More recently, extensions of this law have been presented ([39,40]).

The main characteristic of the above law is that the rotational profile is a monotonic function. However, as anticipated, BNS merger simulations show a rotational profile for the merger remnant incompatible with such trend, and different analytical families have been proposed by Uryū et al. (2017) [15]. One of the main differences is that in these families there is no *one-to-one* relation between Ω and j . In particular, the same rotation rate Ω is associated to different values of the specific angular momentum j .

These rotational profiles can be broadly classified in two families of functions $\Omega = \Omega(j)$: a 3-parameter rotation law (hereafter Uryu3)

$$\Omega(j; p, A, B) = \Omega_c \left[1 + \left(\frac{j}{B^2 \Omega_c} \right)^p \right] \left(1 - \frac{j}{A^2 \Omega_c} \right) \tag{5}$$

and a 4-parameter rotation law (hereafter Uryu4)

$$\Omega(j; p, q, A, B) = \Omega_c \frac{1 + (j/B^2 \Omega_c)^p}{1 + (j/A^2 \Omega_c)^{p+q}} \tag{6}$$

In both the above expressions the index p controls the trend near the rotation axis, which is usually rather flat in BNS simulations, while the index q in Equation (6) controls its asymptotic behavior. In particular, for $q = 3$ one obtains, in the Newtonian limit, a Keplerian rotation. Note that for $B \rightarrow \infty$ Equation (5) reduces to Equation (4).

To handle the difference with respect to one-to-one laws, the integral in Equation (3) must be rewritten as if j were the independent variable according to

$$\int j \, d\Omega = \int j \frac{d\Omega}{dj} \, dj \tag{7}$$

Interestingly, in both Uryu3 and Uryu4 law, the integral is analytical. However hypergeometric functions appear in the integral of the Uryu4 law, and for this reason, all previous studies have been done fixing the parameters p and q to some specific values that allow one to simplify the integral. In particular, the most used combination is $p = 1$ and $q = 3$, and this choice will also be assumed in the present work.

Stationary and axisymmetric purely rotating fluids satisfy the *circularity* condition [41–43], under which the 3 + 1 spacetime line element can be written in spherical coordinates as e.g., [26]

$$ds^2 = -\alpha^2 dt^2 + \psi^4 \left(dr^2 + r^2 d\theta^2 \right) + \mathcal{R}^2 (d\phi - \omega dt)^2 \tag{8}$$

where α is the lapse function, ψ as the conformal factor, \mathcal{R} is the generalized cylindrical radius, and $\omega = -\beta^\phi$ is the angular velocity, as measured by an observer at infinity, of the zero angular momentum observer (ZAMO [44]), responsible for frame dragging. The quantity j then becomes

$$j = u^t u_\phi = \frac{\mathcal{R}^2 (\Omega - \omega)}{\alpha^2 - \mathcal{R}^2 (\Omega - \omega)^2} \tag{9}$$

Under the further assumption of conformal flatness, which was proved to be highly accurate for rotating NS even close to mass shedding [26,27,45], one has $\mathcal{R} = \psi^2 r \sin \theta$.

Equation (9), once the space-time metric and a rotational law have been assumed, allows one to derive $j(\Omega)$, or $\Omega(j)$, as a function of position r and θ . In turn, this allows for the integration of Equation (3) and the determination of the matter distribution inside the star. Once the structure of the star is found, global quantities like mass M and the moment of inertia I , as well as local quantities like the equatorial radius r_e and polar radius r_p , can be determined. For the present work, the physical input parameters that characterize a

particular configuration are the values of the central density ρ_c and central rotation rate Ω_c , other parameters will be discussed in Section 3.

To close the system and solve Equation (3) a (barotropic) EoS is needed. In this work we explore three different possibilities. One is the standard polytropic EoS $p = K\rho^\Gamma$ (Pol2) with an adiabatic index $\Gamma = 2$ and a polytropic constant $K = 110$ (in geometrized units). The other two are tabulated zero-temperature, purely nucleonic EoSs, namely the APR4 [46] and the NL3 $\omega\rho$ [47]. More detailed information, especially on how these are matched to the low density regime, can be found in [32].

3. Equilibrium Configurations and Quadrupole Moments

The equilibrium configurations are computed using an updated version of the XNS code [26,27], employing spherical coordinates and assuming a uniformly spaced grid, with 500 points in the radial coordinate r covering the range $r \in [0, 20]$ and 200 points in the polar angular coordinate θ in the range $\theta \in [0, \pi]$. For all models we impose a central density $\rho_c = 1.28 \times 10^{-3}$ and a central rotation rate $\Omega_c = 2.22 \times 10^{-2}$. The other free parameters are the radial position where the rotation rate reaches the maximum, r_{\max} , and the corresponding value $\Omega_{\max} = \Omega(r_{\max})$, or equivalently the ratio

$$\lambda = \frac{\Omega_{\max}}{\Omega_c} \tag{10}$$

All models considered in this work are reported in Table 1, where the first upper letter refers to the EoS and the number to the Uryū law. Since the Ω_{\max}/Ω_c ratio for a BNS remnants is approximately 2 (e.g., [6,8–10,13]), we computed our models using either $\lambda = 2$ or $\lambda = 1.5$, in order to study the dependence of the properties of the BNS remnants on this particular parameter. To study the dependence on the p parameter in the Uryu3 law, we set $p = 3/2$ and $p = 1$ as in [15,22,23]. The parameter r_{\max} is chosen in order to get the position of the maximum rotation rate within the inner half of the star.

Figure 1a shows the profile of the rotation rate on the equatorial plane for models A3. As it is possible to see, models A3b, A3c and A3d have the same r_{\max}/r_e ratio (where r_e is the equatorial radius of the star), while for the model A3a this ratio is exactly half of that of the previous models. This implies that the equatorial radius is independent of the rotation parameters for $r_{\max} < 1$, as can also be seen in Table 1. This is not true for $r_{\max} > 1$: repeating the simulations with $r_{\max} = 1.5$ and 2.5, and varying the other rotation parameters, we observe a variation of the equatorial radius, implying that the equatorial radius does not depend on the rotation parameters only for $r_{\max} < 1$. However, the equatorial radius depends on the EoS, as it is possible to see in Figure 1b, where the rotation rate on the equatorial plane for models A4e and P4e is shown. These models are computed with the same rotation profile and other parameters, but with a different EoS. We find a different r_{\max}/r_e ratio for these two models, implying a different equatorial radius.

All models in Table 1 present the maximum rest mass density in the center. In Figure 2 we compare the density profile for models 3b and 4b with those of the corresponding non-rotating star, i.e., the static configuration computed with the same EoS and central density of the rotating model. We find that there is no difference between the density shapes plotted with respect the r/r_e ratio, regardless of the rotation profile and parameters. However, this is not an universal shape: in fact, by increasing the central rotation rate or defining other quantities to parametrize the rotation profiles—for example the Ω_e/Ω_c ratio, with Ω_e the equatorial rotation rate—it is possible to obtain a density profile with a maximum away from the center of the star (e.g., [15,21,24,25], see also below).

As can be seen in Table 1, rest (M_0) and Komar (M_K) masses show an increase as r_{\max} and λ increase. They are also very similar for both values of p used for the Uryu3 law in this work and assume higher values for models N and lower values for models A. Their ratio reaches higher values for models N too, but, for a given EoS, it is independent on the parameters of the rotation profile. The circumferential radius R_c assumes similar values for different p and λ , and it increases for increasing r_{\max} , showing a strong dependence on this

parameter. This radius has the lowest values for models A and the highest for models P, while it shows no dependence on the rotation profile (again for a given EoS).

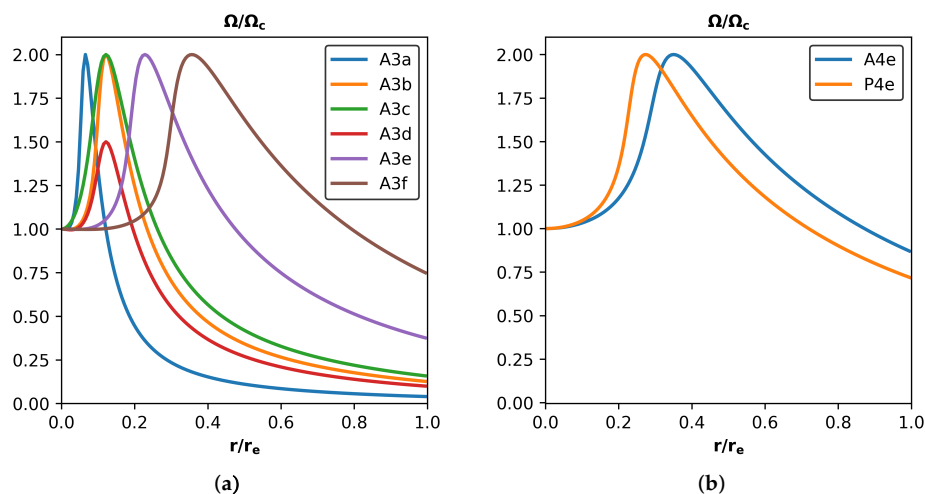


Figure 1. Rotation rate vs. radius on the equatorial plane for (a) models A3 and (b) models 4e in Table 1. Values of the rotation rate are relative to the central value, while values of the radius are relative to the equatorial radius of the star.

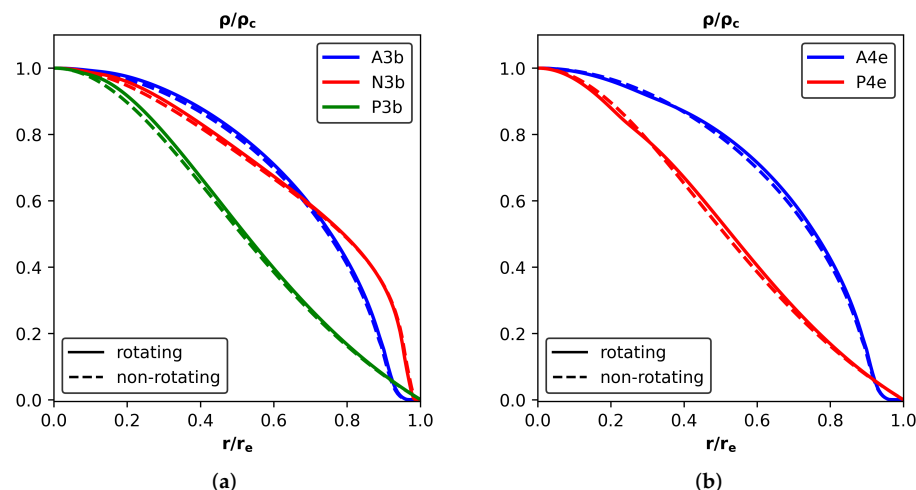


Figure 2. Rest mass density vs. radius on the equatorial plane for (a) models 4b and (b) models 4e in Table 1. Solid (dashed) lines are for the rotating (non-rotating) star. Values of the rest mass density are relative to the central value, while values of the radius are relative to the equatorial radius of the star. See the text for more details.

The moment of inertia I -given by the usual relation [48,49]

$$I = \frac{J}{\Omega_e} \tag{11}$$

increases with all rotation parameters and shows lower values for the Uryu4 law, regardless of the EoS employed. It also reaches higher values for models N and lower values for models A. The equatorial rotation rate Ω_e and the angular momentum J also increase for increasing r_{\max} and λ values, but they both decrease for larger p . In particular, these parameters show a strong dependence on the radial position where Ω reaches the maximum, as can be seen in Figure 1 for the rotation rate, regardless of the EoS. Like for the moment of inertia, they show higher values for models N (for fixed rotation parameters), but the equatorial rotation rate shows the lowest values for models P instead of for models A.

Note that for differential rotators there is an arbitrariness in the definition of the rotational rate that should be used in Equation (11). Given our rotational profiles, Ω_e is typically smaller (possibly much smaller) than both the average and the central rotation rate. As a consequence, the value of the moment of inertia is potentially much higher than for analogous models (with the same rotational kinetic energy) assuming uniform rotation. This introduces important biases on several derived quantities, in particular the ‘effective Newtonian’ quadrupole, that should be properly considered.

Table 1. Physical quantities for all models considered in this work. Listed quantities are (in geometrized units) the radial position where the rotation rate reaches the maximum r_{\max} , the equatorial radius r_e , the circumferential radius R_c , the equatorial rotation rate Ω_e , the angular momentum J , the rest and Komar masses M_0 and M_K , the kinetic-to-gravitational ratio $T/|W|$, and the moment of inertia I . Models A are computed using the APR4 EoS, models N are computed using the NL3 $\omega\rho$ EoS, and models P are computed using the polytropic EoS $p = K\rho^\Gamma$ with $K = 110$ and $\Gamma = 2$. The number in the model name refers to the Uryū law: models 3 are computed using the Uryu3 law with $p = 3/2$ (except for models 3c, computed with $p = 1$), while models 4 are computed using the Uryu4 law with $(p, q) = (1, 3)$. All models are computed with $\lambda = 2$ (except for models 3d and 4c computed with $\lambda = 1.5$), and have a central density $\rho_c = 1.28 \times 10^{-3}$ and a central rotation rate $\Omega_c = 2.22 \times 10^{-2}$.

Model	r_{\max}	r_e	R_c	Ω_e ($\times 10^{-3}$)	J ($\times 10^{-1}$)	M_0	M_K	$T/ W $ ($\times 10^{-3}$)	I ($\times 10$)
A3a	0.4	6.42	7.59	0.88	0.528	1.214	1.122	0.86	6.008
A3b	0.8	6.42	7.62	2.79	1.645	1.240	1.145	6.02	5.897
A3c	0.8	6.42	7.63	3.49	2.022	1.250	1.154	8.30	5.800
A3d	0.8	6.42	7.60	2.20	1.270	1.225	1.133	3.71	5.784
A3e	1.5	6.58	7.87	8.28	4.926	1.322	1.219	32.4	5.950
A3f	2.5	7.02	8.48	16.5	10.53	1.467	1.351	84.3	6.376
A4a	0.4	6.42	7.60	2.02	0.958	1.218	1.127	2.00	4.750
A4b	0.8	6.46	7.67	4.83	2.348	1.251	1.156	9.81	4.864
A4c	0.8	6.46	7.65	3.70	1.764	1.232	1.138	5.88	4.764
A4d	1.5	6.66	7.98	11.2	5.889	1.346	1.240	40.4	5.277
A4e	2.5	7.14	8.63	19.2	11.72	1.502	1.382	93.3	6.096
N3a	0.4	6.50	9.34	2.54	5.195	3.083	2.582	2.66	20.42
N3b	0.8	6.50	9.41	6.98	14.04	3.138	2.628	15.1	20.11
N3c	0.8	6.50	9.43	8.31	16.51	3.158	2.645	19.5	19.86
N3d	0.8	6.50	9.37	5.32	10.51	3.106	2.602	8.81	19.76
N4a	0.4	6.50	9.35	4.36	7.885	3.093	2.591	5.03	18.10
N4b	0.8	6.50	9.44	9.50	17.42	3.161	2.648	20.6	18.33
N4c	0.8	6.50	9.39	7.15	12.82	3.118	2.612	11.8	17.93
P3a	0.4	8.22	9.81	0.69	0.928	1.644	1.522	0.88	13.51
P3b	0.8	8.22	9.84	2.17	2.864	1.668	1.543	6.17	13.20
P3c	0.8	8.22	9.85	2.71	3.520	1.678	1.552	8.53	12.97
P3d	0.8	8.22	9.83	1.70	2.220	1.655	1.533	3.78	13.03
P3e	1.5	8.30	10.0	6.59	8.605	1.769	1.635	33.6	13.07
P3f	2.5	8.90	10.9	13.2	19.67	2.005	1.848	90.9	14.86
P4a	0.4	8.22	9.82	1.66	1.735	1.649	1.527	2.11	10.47
P4b	0.8	8.22	9.86	3.98	4.203	1.682	1.557	10.3	10.56
P4c	0.8	8.26	9.87	3.02	3.171	1.664	1.540	6.16	10.49
P4d	1.5	8.42	10.2	9.26	10.58	1.805	1.667	43.0	11.42
P4e	2.5	9.14	11.2	15.9	22.63	2.068	1.904	103	14.24

The kinetic-to-gravitational energy ratio $T/|W|$ shows the same dependence on the rotation profile and the angular momentum parameters. Also this quantity strongly depends on r_{\max} , but the dependence on the other rotation parameters is not negligible. In none of the model that we have investigated this ratio exceeds 0.27, which is the typical threshold value against bar-mode instability [22,23,50]. Thus, we can safely assume that our models represent stable configurations, also in consideration of the fact that a proper threshold for differentially rotating system is likely to hold at a higher value.

Apart from the trends in the global parameters, it is also important to investigate and characterize the deformation of our configurations, in the light of possible GW emission. In this respect, we have considered three quantities of interest: the ratio of the polar to equatorial radius, characterizing the deformation of the star, the Newtonian quadrupole deformation e -defined as

$$e = \frac{I_{zz} - I_{xx}}{I_{zz}} \tag{12}$$

where I_{zz} and I_{xx} are the Newtonian moments of inertia around the polar axis z and the x axis, respectively-and the metric quadrupole Q -defined as

$$Q = \sqrt{5\pi} \int_0^\pi r^3 \ln(\alpha) Y_2(\theta) \sin \theta d\theta \tag{13}$$

where $Y_2(\theta)$ is the spherical harmonic function of order 2 (with $m = 0$), and integration is performed for radii $r > R_c$ (see Table 2). Note that in CFC this is equivalent to the Thorne quadrupole [51,52], that is the relevant quantity for GW emission, the difference between the two being proportional to the deviation from conformal flatness. For uniformly rotating NS even at mass shedding we have verified, using uniformly rotating model computed in quasi-isotropic coordinates [53], that the difference is less than a few percent.

Table 2. Polar-to-equatorial ratio r_p/r_e , Newtonian quadrupole deformation e -defined by Equation (12), distortion coefficient a_Ω -defined by Equation (14) and metric quadrupole Q -defined by Equation (13), for all models in Table 1.

Model	r_p/r_e	e	a_Ω	Q
A3a	0.99	0.003	3.4	0.04
A3b	0.96	0.020	3.3	0.26
A3c	0.96	0.027	3.2	0.36
A3d	0.98	0.012	3.3	0.16
A3e	0.87	0.095	2.9	1.45
A3f	0.75	0.212	2.5	4.20
A4a	0.98	0.007	3.3	0.09
A4b	0.94	0.031	3.2	0.42
A4c	0.96	0.019	3.2	0.25
A4d	0.85	0.115	2.9	1.83
A4e	0.73	0.229	2.5	4.77
N3a	0.98	0.008	3.1	0.31
N3b	0.93	0.042	2.8	1.73
N3c	0.91	0.053	2.7	2.25
N3d	0.96	0.025	2.8	1.03
N4a	0.97	0.015	2.9	0.57
N4b	0.91	0.055	2.7	2.40
N4c	0.95	0.033	2.8	1.39
P3a	0.99	0.003	3.2	0.07
P3b	0.96	0.019	3.1	0.48
P3c	0.94	0.026	3.0	0.66
P3d	0.97	0.012	3.1	0.30
P3e	0.87	0.094	2.8	2.69
P3f	0.72	0.219	2.4	8.44
P4a	0.98	0.007	3.2	0.16
P4b	0.94	0.032	3.1	0.81
P4c	0.96	0.019	3.1	0.48
P4d	0.83	0.118	2.7	3.53
P4e	0.68	0.242	2.3	9.99

All the mentioned quantities show a dependence on r_{\max} (see Table 2). In particular, the Newtonian quadrupole deformation and the metric quadrupole show a strong dependence on each rotation parameter regardless of the EoS, while the polar-to-equatorial ratio

show a strong dependence on r_{\max} only. As the angular momentum and the kinetic-to-gravitational ratio, both quadrupole deformation and metric quadrupole show, for fixed rotation profile and parameters, a strong dependence on the EoS; in particular, they show higher values for models N and lower values for models A. We also found that, for all our models, the metric quadrupole Q is about $(0.30 \pm 0.05) \times Ie$. Interestingly, this agrees with what was found in [54], where it was shown that typically Q was equal to 0.4–0.5 times Ie . The slightly lower coefficient that we find in this case, can be attributed partly to the bias in the definition of the moment of inertia that we have discussed above. This however confirms that the combined use of the GR moment of inertia, for which, in the case of uniform rotators, one can adopt the quasi-universal relation in [49], together with the Newtonian deformation rate, that can be easily computed on stellar model without the need of complex asymptotic metric extrapolations, can be used as a reliable proxy for the full GR quadrupole (see the recent work [55]). Interestingly, this agrees with what found for non-rotating magnetized NSs [54].

It is known that both in the Newtonian limit [56] and in GR [52], the quadrupole deformation can be rewritten using the perturbative formula (in the limit of small Ω_c)

$$e = a_{\Omega} \frac{T}{|W|} + \mathcal{O}\left(\left(\frac{T}{|W|}\right)^2\right) \tag{14}$$

where a_{Ω} is called the ‘distortion coefficient’. As can be seen in Table 2, this coefficient has the lowest values for models N and the highest for models A, and does not show a strong dependence on the rotation parameters. As a function of the mass of the star, we found a quasi-linear decrease in the distortion coefficient as the rest mass (or equivalently the Komar mass) increased, regardless of the EoS. However a_{Ω} vary in a narrow range between 2.5 and 3.5. This is in agreement with Pili et al. (2017) [19] where it was found that for uniform rotators and the Pol2 EoS $a_{\Omega} \simeq 3.7$ through the entire stable mass range. It also agrees with the recent findings by Soldateschi et al. [32] on the magnetic deformability of NS, suggesting the the distortion coefficient, once the deformation is parametrized in terms of energy ratio, can be safely assumed to be almost constant, and typically in the range 2.5–4.

As mentioned above, a different combination of rotation parameters or central rotation rate can lead to a different star shape [15,21,24,25]. The two possible shapes are: (1) a star with the maximum density in the center, or (2) a star with the maximum density away from the center. All models in Table 1 are stars of the first type, i.e., with the maximum density in the center, as seen above. To study the dependence of the quadrupole deformation and the metric quadrupole on the central rotation rate and the star shape, we computed a new model-labeled $A4b_b$ -with the same rotation law and parameters as model $A4b$ but with a double central rotation rate. Figure 3 show the rest mass density distribution for both $A4b$ and $A4b_b$ models. As it is possible to see, model $A4b_b$ show a density distribution with a maximum value away from the center, at $r/r_e = 0.1743$, and a ratio $\rho_{\max}/\rho_c = 1.0055$. Comparing the quantities for model $A4b$ (Tables 1 and 2) with those for model $A4b_b$ (Table 3), it is possible to see that all the quantities (except the polar-to-equatorial ratio) are greater for model $A4b_b$. This implies a strong dependence on the central rotation rate, as expected, and on the shape of the star. It is important to note that in this case the linear approximation (14) for the quadrupole deformation is no longer valid. In fact, by fitting data obtained with simulations computed using a central rotation rate varying between 1/8 and 2 times that of the model $A4b$, we found that the perturbative formula (14) is a good approximation for the quadrupole deformation for central rotation rates up to approximately the nominal value used for model $A4b$, while for higher values the quadratic order on the perturbative formula is required, i.e., Equation (14) must be rewritten as

$$e = a_{\Omega} \frac{T}{|W|} + b_{\Omega} \left(\frac{T}{|W|}\right)^2 + \mathcal{O}\left(\left(\frac{T}{|W|}\right)^3\right) \tag{15}$$

with $a_\Omega = 3.296 \pm 0.004$ and $b_\Omega = -11.5 \pm 0.1$.

Table 3. Physical quantities (see Tables 1 and 2 for their definitions) for model A4b_b (same rotation law and parameters as model A4b but with a double central rotation rate (see the text for more details)).

r_e	R_c	Ω_e ($\times 10^{-3}$)	J ($\times 10^{-1}$)	M_0	M_K	$T/ W $ ($\times 10^{-3}$)	I ($\times 10$)	r_p/r_e	e	Q
6.54	7.94	10.3	6.162	1.432	1.312	40.7	5.984	0.80	0.115	1.90

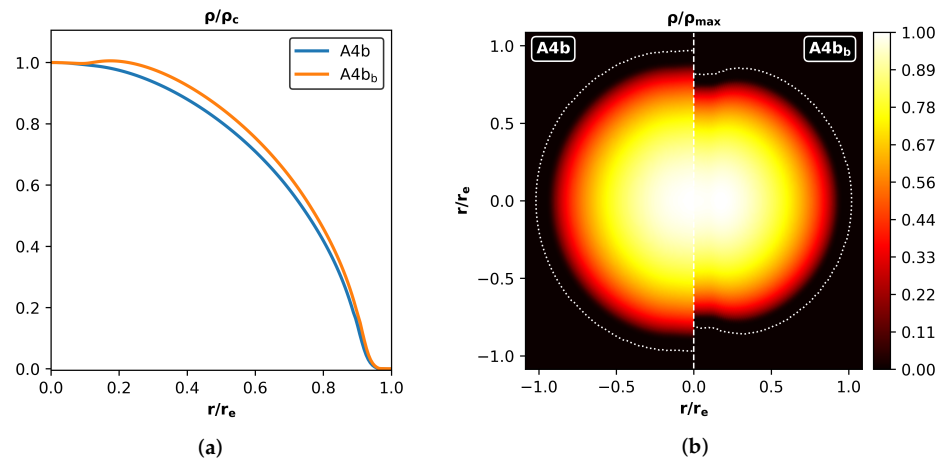


Figure 3. Rest mass density vs. radius (a) and two-dimensional rest mass density distribution (b) for models A4b and A4b_b. Values of the rest mass density are relative to the central value in (a) and to the maximum value in (b), while values of the radii are relative to the equatorial radius. The left (right) side of (b) show the distribution for model A4b (A4b_b). The white dotted lines are the surface of the stars.

4. Summary and Conclusions

In this work we investigated the dependence of the quadrupole deformation, the metric quadrupole, and other physical quantities like mass and angular momentum, of rotating relativistic stars, modeled as equilibrium configurations with realistic post-merger rotation profiles. We computed our models using the XNS code [26,27], in which we have implemented the rotation profiles proposed by Uryū et al. [15], and employing three different Equations of State (EoSs).

We found that the equatorial radius of the star is independent on the rotation parameters if the radial position r_{\max} where the rotation rate reaches its maximum value is lower than one (in geometrized units), regardless of the EoS assumed. Values of rotational quantities (such as angular momentum and equatorial rotation rate) tend to be higher for the Uryū law with four parameters than for the law with three parameters. Masses, quadrupole deformation, metric quadrupole and rotational quantities all show an increase as the ratio between the maximum value of the rotation rate Ω_{\max} and its central value Ω_c increases, and similarly with respect to r_{\max} . These rotational quantities also show higher values for the NL3 $\omega\rho$ EoS and lower values for the APR4 EoS, except the equatorial rotation rate showing lower values for the Polytropic (Pol2) EoS.

We also found that the quadrupole deformation $e = 1 - I_{xx}/I_{zz}$ can be approximated reasonably well with a perturbative formula to the first order in $T/|W|$ (the kinetic-to-gravitational energy ratio), provided the central rotation rate is not higher than the values considered in the present work, otherwise the second order term in the expansion becomes necessary (see Equations (14) and (15)). Notice that the quadrupole deformation of our models is always positive. However, very strong magnetic fields could make this parameter negative, as shown, for example, in [30].

Models such as those studied in this work, with the addition of magnetic fields (always possible using the XNS code), can represent an initial condition for time-dependent

studies with GRMHD codes such as ECHO [33], in order to investigate, for instance, the amplification of magnetic fields in this kind of sources due to mechanisms such as the magnetorotational instability (MRI) or the (mean-field) dynamo [57]. We leave such investigations as future work.

Author Contributions: Conceptualization, K.F., L.D.Z. and N.B.; data curation, K.F. and J.S.; writing—original draft, K.F.; writing—review and editing, L.D.Z. and N.B. All authors have read and agreed to the published version of the manuscript.

Funding: This research received no external funding.

Data Availability Statement: Not applicable.

Acknowledgments: The authors thank R. De Pietri for useful discussion.

Conflicts of Interest: The authors declare no conflict of interest.

Appendix A. Implementation of the Uryū Laws in the XNS Code

Here we provide details of the implementation of the profiles by Uryū in the last version of the XNS code. The needed parameters are the values of (p, λ, r_{\max}) for the Uryu3 law and of $(p, q, \lambda, r_{\max})$ for the Uryu4 law (see Section 3 for the definitions of λ and r_{\max}). To simplify the notation we first define the following quantities

$$\bar{\Omega} = \frac{\Omega}{\Omega_c}, \quad J = \frac{j}{j_{\max}}, \quad x = \frac{j_{\max}}{A^2 \Omega_c}, \quad y = \left(\frac{j_{\max}}{B^2 \Omega_c} \right)^p \tag{A1}$$

where j_{\max} is the value of j at r_{\max} , when $\Omega = \Omega_{\max}$, which can be evaluated using Equation (9). We can thus rewrite Equations (5) and (6) as, respectively

$$\bar{\Omega}(J; p, x, y) = (1 + yJ^p)(1 - xJ) \tag{A2}$$

and

$$\bar{\Omega}(J; p, q, x, y) = \frac{1 + yJ^p}{1 + (xJ)^{p+q}} \tag{A3}$$

and the integral (7) is now computed as

$$I = \int_0^J j' \frac{d\Omega}{dj'} dj' = \Omega_c j_{\max} \int_0^J J' \frac{d\bar{\Omega}}{dJ'} dJ' \tag{A4}$$

With these definitions when $\Omega = \Omega_{\max}$ we have $J = 1, \bar{\Omega} = \lambda$, and a vanishing derivative $d\bar{\Omega}/dJ = 0$. Note that, by definition, all parameters J, x, y, p and q cannot be negative.

Appendix A.1. The Uryu3 Law

The first derivative of Equation (A2) is

$$\frac{d\bar{\Omega}}{dJ} = -x + pyJ^{p-1} - (p + 1)xyJ^p \tag{A5}$$

The condition at the maximum point tells us that

$$y = \frac{x}{p - (p + 1)x} \tag{A6}$$

Notice that the condition $y > 0$ implies

$$x < \frac{p}{p + 1} \tag{A7}$$

From Equation (A2) it follows that at the maximum point we have

$$y = \frac{\lambda}{1-x} - 1 \tag{A8}$$

By equating Equations (A6) and (A8) we then obtain

$$x = \frac{2p - \lambda(p+1) \pm \sqrt{\Delta}}{2p} \tag{A9}$$

with

$$\Delta = \lambda^2(p+1)^2 - 4p\lambda \tag{A10}$$

Real solutions exist for

$$\lambda \geq \frac{4p}{(p+1)^2} \tag{A11}$$

For $\lambda > 1$, $\Delta > 0$ and only the solution with positive sign in Equation (A9) respects the condition $x > 0$, so we have

$$x = \frac{2p - \lambda(p+1) + \sqrt{\Delta}}{2p} \tag{A12}$$

From the study of the second derivative of $\bar{\Omega}$ (which must be negative at the maximum point) we obtain the constraint

$$x > \frac{p-1}{p+1} \tag{A13}$$

In summary, x is given by Equation (A12) with constraints (A7) and (A13), while y is given by Equation (A8) or equivalently by Equation (A6). Finally, the integral (A4) results to be

$$I = -\Omega_c j_{\max} \left[\frac{x}{2} J^2 - \frac{py}{p+1} J^{p+1} + \frac{p+1}{p+2} xy J^{p+2} \right] \tag{A14}$$

The procedure used to implement the Uryu3 law in the XNS code is therefore the following:

1. initialization of the values of the parameters Ω_c , Ω_{\max} , r_{\max} and p ;
2. evaluation of λ and j_{\max} ;
3. evaluation of x and y using Equations (A12) and (A8) respectively;
4. resolution (The XNS code finds the zeros of the function via an iterative Newton's method.) of Equation (A2) with j given by Equation (9) to find the value of Ω ;
5. evaluation of the integral (A14).

Steps 4 and 5 are repeated for each grid point.

Appendix A.2. The Uryu4 Law

The first derivative of Equation (A3) is

$$\frac{d\bar{\Omega}}{dJ} = py \frac{J^{p-1}}{(1+x_1 J^{p+q})} - (p+q)x_1 \frac{1+yJ^p}{(1+x_1 J^{p+q})^2} J^{p+q-1} \tag{A15}$$

where $x_1 = x^{p+q}$, and from equation (A3) it follows that at the point of the maximum we have

$$1+y = \lambda(1+x_1) \tag{A16}$$

Combining the vanishing of the derivative in Equation (A15) with the above condition we easily get

$$x = \left(\frac{\lambda-1}{\lambda} \frac{p}{q} \right)^{\frac{1}{p+q}}, \quad y = \frac{p+q}{q} (\lambda-1) \tag{A17}$$

Notice that these value of x and y are both positive for all $\lambda > 1$. For the chosen values $(p, q) = (1, 3)$, we have in particular

$$x = \left(\frac{\lambda - 1}{3\lambda} \right)^{1/4}, \quad y = \frac{4}{3}(\lambda - 1) \quad (\text{A18})$$

Setting $k = xJ$, the integral (A4) results to be

$$I = j\Omega - \frac{\sqrt{2}\Omega_c j_{\max}}{4x} \left[\frac{\sqrt{2}y}{x} \tan^{-1}(k^2) + \tan^{-1}(1 + \sqrt{2}k) - \tan^{-1}(1 - \sqrt{2}k) + \tanh^{-1}\left(\frac{\sqrt{2}k}{1 + k^2}\right) \right] \quad (\text{A19})$$

The procedure used to implement the Uryu4 law in the XNS code, with the choice of parameters $p = 1$ and $q = 3$ providing the above analytical integral, is therefore the following:

1. initialization of the values of the parameters Ω_c , Ω_{\max} and r_{\max} ;
2. evaluation of λ and j_{\max} ;
3. evaluation of x and y using Equations (A18);
4. resolution of Equation (A3) with j given by Equation (9) to find the value of Ω ;
5. evaluation of the integral (A19).

Steps 4 and 5 are repeated for each grid point.

References

1. Abbott, B.P. GW170817: Observation of Gravitational Waves from a Binary Neutron Star Inspiral. *Phys. Rev. Lett.* **2017**, *119*, 161101. [[CrossRef](#)] [[PubMed](#)]
2. Abbott, B.P. Multi-messenger Observations of a Binary Neutron Star Merger. *Astrophys. J. Lett.* **2017**, *848*, L12. [[CrossRef](#)]
3. Bailes, M. Gravitational-wave physics and astronomy in the 2020s and 2030s. *Nat. Rev. Phys.* **2021**, *3*, 344–366. [[CrossRef](#)]
4. Hotokezaka, K.; Kyutoku, K.; Okawa, H.; Shibata, M.; Kiuchi, K. Binary neutron star mergers: Dependence on the nuclear equation of state. *Phys. Rev. D* **2011**, *83*, 124008. [[CrossRef](#)]
5. Sekiguchi, Y.; Kiuchi, K.; Kyutoku, K.; Shibata, M. Gravitational Waves and Neutrino Emission from the Merger of Binary Neutron Stars. *Phys. Rev. Lett.* **2011**, *107*, 051102. [[CrossRef](#)] [[PubMed](#)]
6. Kastaun, W.; Galeazzi, F. Properties of hypermassive neutron stars formed in mergers of spinning binaries. *Phys. Rev. D* **2015**, *91*, 064027. [[CrossRef](#)]
7. De Pietri, R.; Feo, A.; Maione, F.; Löffler, F. Modeling equal and unequal mass binary neutron star mergers using public codes. *Phys. Rev. D* **2016**, *93*, 064047. [[CrossRef](#)]
8. Ciolfi, R.; Kastaun, W.; Giacomazzo, B.; Endrizzi, A.; Siegel, D.M.; Perna, R. General relativistic magnetohydrodynamic simulations of binary neutron star mergers forming a long-lived neutron star. *Phys. Rev. D* **2017**, *95*, 063016. [[CrossRef](#)]
9. Kiuchi, K.; Kyutoku, K.; Sekiguchi, Y.; Shibata, M. Global simulations of strongly magnetized remnant massive neutron stars formed in binary neutron star mergers. *Phys. Rev. D* **2018**, *97*, 124039. [[CrossRef](#)]
10. Ciolfi, R.; Kastaun, W.; Kalinani, J.V.; Giacomazzo, B. First 100 ms of a long-lived magnetized neutron star formed in a binary neutron star merger. *Phys. Rev. D* **2019**, *100*, 023005. [[CrossRef](#)]
11. De Pietri, R.; Feo, A.; Font, J.A.; Löffler, F.; Pasquali, M.; Stergioulas, N. Numerical-relativity simulations of long-lived remnants of binary neutron star mergers. *Phys. Rev. D* **2020**, *101*, 064052. [[CrossRef](#)]
12. Mösta, P.; Radice, D.; Haas, R.; Schnetter, E.; Sebastiano Bernuzzi, S. A magnetar engine for short GRBs and kilonovae. *Astrophys. J. Lett.* **2020**, *901*, L37. [[CrossRef](#)]
13. Kastaun, W.; Ohme, F. Numerical inside view of hypermassive remnant models for GW170817. *Phys. Rev. D* **2021**, *104*, 023001. [[CrossRef](#)]
14. Nedora, V.; Bernuzzi, S.; Radice, D.; Daszuta, B.; Endrizzi, A.; Perego, A.; Prakash, A.; Safarzadeh, M.; Schianchi, F.; Logoteta, D. Numerical Relativity Simulations of the Neutron Star Merger GW170817: Long-term Remnant Evolutions, Winds, Remnant Disks, and Nucleosynthesis. *Astron. J.* **2021**, *906*, 98. [[CrossRef](#)]
15. Uryū, K.; Tsokaros, A.; Baiotti, L.; Galeazzi, F.; Taniguchi, K.; Yoshida, S. Modeling differential rotations of compact stars in equilibriums. *Phys. Rev. D* **2017**, *96*, 103011. [[CrossRef](#)]
16. Galeazzi, F.; Yoshida, S.; Eriguchi, Y. Differentially-rotating neutron star models with a parametrized rotation profile. *Phys. Rev. D* **2012**, *85*, A156. [[CrossRef](#)]
17. Cameli, G.; Dietrich, T.; Rosswog, S.; Haskell, B. Axisymmetric models for neutron star merger remnants with realistic thermal and rotational profiles. *Phys. Rev. D* **2021**, *103*, 063014. [[CrossRef](#)]

18. Bonazzola, S.; Gourgoulhon, E.; Salgado, M.; Marck, J.A. Axisymmetric rotating relativistic bodies: A new numerical approach for 'exact' solutions. *Astron. Astrophys.* **1993**, *278*, 421–443.
19. Pili, A.G.; Bucciantini, N.; Del Zanna, L. General relativistic models for rotating magnetized neutron stars in conformally flat space-time. *Mon. Not. R. Astron. Soc.* **2017**, *470*, 2469–2493. [[CrossRef](#)]
20. Camelió, G.; Dietrich, T.; Marques, M.; Rosswog, S. Rotating neutron stars with nonbarotropic thermal profile. *Phys. Rev. D* **2019**, *100*, 123001. [[CrossRef](#)]
21. Zhou, E.; Tsokaros, A.; Uryū, K.; Xu, R.; Shibata, M. Differentially rotating strange star in general relativity. *Phys. Rev. D* **2019**, *100*, 043015. [[CrossRef](#)]
22. Passamonti, A.; Andersson, N. Merger-inspired rotation laws and the low-T/W instability in neutron stars. *Mon. Not. R. Astron. Soc.* **2020**, *498*, 5904–5915. [[CrossRef](#)]
23. Xie, X.; Hawke, I.; Passamonti, A.; Andersson, N. Instabilities in neutron-star postmerger remnants. *Phys. Rev. D* **2020**, *102*, 044040. [[CrossRef](#)]
24. Iosif, P.; Stergioulas, N. Equilibrium sequences of differentially rotating stars with post-merger-like rotational profiles. *Mon. Not. R. Astron. Soc.* **2021**, *503*, 850–866. [[CrossRef](#)]
25. Iosif, P.; Stergioulas, N. Models of binary neutron star remnants with tabulated equations of state. *Mon. Not. R. Astron. Soc.* **2022**, *510*, 2948–2967. [[CrossRef](#)]
26. Bucciantini, N.; Del Zanna, L. GRMHD in axisymmetric dynamical spacetimes—the X-ECHO code. *Astron. Astrophys.* **2011**, *528*, A101. [[CrossRef](#)]
27. Pili, A.G.; Bucciantini, N.; Del Zanna, L. Axisymmetric equilibrium models for magnetized neutron stars in General Relativity under the Conformally Flat Condition. *Mon. Not. R. Astron. Soc.* **2014**, *439*, 3541–3563. [[CrossRef](#)]
28. Cordero-Carrión, I.; Cerdá-Durán, P.; Dimmelmeier, H.; Jaramillo, J.L.; Novak, J.; Gourgoulhon, E. Improved constrained scheme for the Einstein equations: An approach to the uniqueness issue. *Phys. Rev. D* **2009**, *79*, 024017. [[CrossRef](#)]
29. Bucciantini, N.; Pili, A.G.; Del Zanna, L. The role of currents distribution in general relativistic equilibria of magnetized neutron stars. *Mon. Not. R. Astron. Soc.* **2015**, *447*, 3278–3290. [[CrossRef](#)]
30. Soldateschi, J.; Bucciantini, N.; Del Zanna, L. Axisymmetric equilibrium models for magnetised neutron stars in scalar-tensor theories. *Astron. Astrophys.* **2020**, *640*, A44. [[CrossRef](#)]
31. Soldateschi, J.; Bucciantini, N.; Del Zanna, L. Magnetic deformation of neutron stars in scalar-tensor theories. *Astron. Astrophys.* **2021**, *645*, A39. [[CrossRef](#)]
32. Soldateschi, J.; Bucciantini, N.; Del Zanna, L. Quasi-universality of the magnetic deformation of neutron stars in general relativity and beyond. *Astron. Astrophys.* **2021**, *654*, A162. [[CrossRef](#)]
33. Del Zanna, L.; Zanotti, O.; Bucciantini, N.; Londrillo, P. ECHO: An Eulerian Conservative High Order scheme for general relativistic magnetohydrodynamics and magnetodynamics. *Astron. Astrophys.* **2007**, *473*, 11–30. [[CrossRef](#)]
34. Franceschetti, K.; Del Zanna, L. General Relativistic Mean-Field Dynamo Model for Proto-Neutron Stars. *Universe* **2020**, *6*, 83. [[CrossRef](#)]
35. Komatsu, H.; Eriguchi, Y.; Hachisu, I. Rapidly rotating general relativistic stars. I-Numerical method and its application to uniformly rotating polytropes. *Mon. Not. R. Astron. Soc.* **1989**, *237*, 355–379. [[CrossRef](#)]
36. Stergioulas, N. Rotating Stars in Relativity. *Living Rev. Relativ.* **2003**, *6*, 3. [[CrossRef](#)] [[PubMed](#)]
37. Stergioulas, N.; Apostolatos, T.A.; Font, J.A. Non-linear pulsations in differentially rotating neutron stars: Mass-shedding-induced damping and splitting of the fundamental mode. *Mon. Not. R. Astron. Soc.* **2004**, *352*, 1089–1101. [[CrossRef](#)]
38. Espino, P.L.; Paschalidis, V. Revisiting the maximum mass of differentially rotating neutron stars in general relativity with realistic equations of state. *Phys. Rev. D* **2019**, *99*, 083017. [[CrossRef](#)]
39. Bauswein, A.; Stergioulas, N. Semi-analytic derivation of the threshold mass for prompt collapse in binary neutron-star mergers. *Mon. Not. R. Astron. Soc.* **2017**, *471*, 4956–4965. [[CrossRef](#)]
40. Bozzola, G.; Stergioulas, N.; Bauswein, A. Universal relations for differentially rotating relativistic stars at the threshold to collapse. *Mon. Not. R. Astron. Soc.* **2018**, *474*, 3557–3564. [[CrossRef](#)]
41. Carter, B. The commutation property of a stationary, axisymmetric system. *Commun. Math. Phys.* **1970**, *17*, 233–238. [[CrossRef](#)]
42. Carter, B. Black Hole Equilibrium States. In *Black holes (Les astres occlus)*; DeWitt, C., DeWitt, B.S., Eds.; Gordon and Breach: New York, NY, USA, 1973; pp. 57–214.
43. Gourgoulhon, E.; Markakis, C.; Uryū, K.; Eriguchi, Y. Magnetohydrodynamics in stationary and axisymmetric spacetimes: A fully covariant approach. *Phys. Rev. D* **2011**, *83*, 104007. [[CrossRef](#)]
44. Bardeen, J.M.; Press, W.H.; Teukolsky, S.A. Rotating Black Holes: Locally Nonrotating Frames, Energy Extraction, and Scalar Synchrotron Radiation. *Astrophys. J.* **1972**, *178*, 347–369. [[CrossRef](#)]
45. Iosif, P.; Stergioulas, N. On the accuracy of the IWM–CFC approximation in differentially rotating relativistic stars. *Gen. Relativ. Gravit.* **2014**, *86*, 1800. [[CrossRef](#)]
46. Akmal, A.; Pandharipande, V.R.; Ravenhall, D.G. Equation of state of nucleon matter and neutron star structure. *Phys. Rev. C* **1998**, *58*, 1804. [[CrossRef](#)]
47. Fortin, M.; Providencia, C.; Raduta, A.R.; Gulminelli, F.; Zdunik, J.L.; Haensel, P.; Bejger, M. Neutron star radii and crusts: Uncertainties and unified equations of state. *Phys. Rev. C* **2016**, *94*, 035804. [[CrossRef](#)]

48. Urbanec, M.; Miller, J.C.; Stuchlík, Z. Quadrupole moments of rotating neutron stars and strange stars. *Mon. Not. R. Astron. Soc.* **2013**, *433*, 1903–1909. [[CrossRef](#)]
49. Breu, C.; Rezzolla, L. Maximum mass, moment of inertia and compactness of relativistic star. *Mon. Not. R. Astron. Soc.* **2016**, *459*, 646–656. [[CrossRef](#)]
50. Cerdá-Durán, P.; Quilis, V.; Font, J.A. AMR simulations of the low bar-mode instability of neutron stars. *Comput. Phys. Commun.* **2007**, *177*, 288–297. [[CrossRef](#)]
51. Thorne, K.S. Multipole expansions of gravitational radiation. *Rev. Mod. Phys.* **1980**, *52*, 299. [[CrossRef](#)]
52. Friebe, J.; Rezzolla, L. Equilibrium models of relativistic stars with a toroidal magnetic field. *Mon. Not. R. Astron. Soc.* **2012**, *427*, 3406–3426. [[CrossRef](#)]
53. Stergioulas, N.; Friedman, J.L. Comparing Models of Rapidly Rotating Relativistic Stars Constructed by Two Numerical Methods. *Astrophys. J.* **1995**, *444*, 306. [[CrossRef](#)]
54. Pili, A.; Bucciantini, N.; Del Zanna, L. General relativistic neutron stars with twisted magnetosphere. *Mon. Not. R. Astron. Soc.* **2015**, *447*, 2821–2835. [[CrossRef](#)]
55. Soldateschi, J.; Bucciantini, N. Detectability of Continuous Gravitational Waves from Magnetically Deformed Neutron Stars. *Galaxies* **2021**, *9*, 101. [[CrossRef](#)]
56. Cutler, C. Gravitational Waves from Neutron Stars with Large Toroidal B-fields. *Phys. Rev. D* **2002**, *66*, 084025. [[CrossRef](#)]
57. Del Zanna, L.; Tomei, N.; Franceschetti, K.; Bugli, M.; Bucciantini, N. General Relativistic Magnetohydrodynamics Mean-Field Dynamics. *Fluids* **2022**, *7*, 87. [[CrossRef](#)]